THE ASTROPHYSICAL JOURNAL, 535:833–846, 2000 June 1


# THE MOLECULAR OUTFLOW AND POSSIBLE PRECESSING JET FROM THE MASSIVE YOUNG STELLAR OBJECT IRAS 20126+4104

D. S. SHEPHERD,[1,2] K. C. YU,[3] J. BALLY,[3] AND L. TESTI[2,4]
*Received 1999 September 11; accepted 2000 January 18*

## ABSTRACT

We present images of the molecular gas in the IRAS 20126+4104 massive outflow and examine the interaction between the energetic outflowing material and the surrounding molecular cloud. Mosaic interferometric images in CO(1–0), $^{13}$CO(1–0), C$^{18}$O(1–0), C$^{17}$O(1–0), and millimeter continuum emission are compared with mid-infrared images at 12.5 and 17.9 $\mu$m, near-infrared images in the K$_s$ band (2.17 $\mu$m) and H$_2$ line emission, and optical H$\alpha$ and [S II] images. We show that the molecular outflow is approximately $6 \times 10^4$ yr old with a mass of about 50–60 $M_\odot$ and mass outflow rate $\dot{M}_f \sim 8 \times 10^{-4}$ $M_\odot$ yr$^{-1}$. The driving source is located near the center of the $\gtrsim$300 $M_\odot$ molecular cloud, and the mass of the disk plus circumstellar envelope traced by millimeter continuum emission is $\sim$50 $M_\odot$. The outflow appears to be bounded on most sides by higher density gas traced by C$^{18}$O emission. Shocks identified by H$_2$ and [S II] emission knots follow a NW-SE jet close to the young stellar object and then rotate more north-south along the edges of the CO flow. The most likely interpretation appears to be that the knots trace the working surfaces of a collimated jet that precesses through an angle of $\sim$45°. Possible mechanisms that could produce the jet precession include tidal interactions between the disk and a companion star in a noncoplanar orbit or an anisotropic accretion event that dramatically altered the angular momentum vector of the disk.

*Subject headings:* H II regions — ISM: jets and outflows — ISM: molecules — stars: formation

## 1. INTRODUCTION

Energetic molecular outflows from massive protostars share some characteristics with their low-mass counterparts. In particular, both massive and low-mass flows are probably powered by disk accretion, and the flow energetics scale with the luminosity of the source (see Cabrit & Bertout 1992; Shepherd & Churchwell 1996; Richer et al. 2000). However, the details of the interaction between accretion and outflow are poorly understood, and it is not clear whether outflows from high and low-mass protostars are powered by the same mechanism (e.g., Rodríguez 1995; Cabrit, Raga, & Gueth 1997; Bachiller & Tafalla 1999; Königl & Pudritz 2000; Shu et al. 2000; Eislöffel et al. 2000; Richer et al. 2000). To address this problem, the properties of outflows from luminous young stellar objects at a range of evolutionary stages must be studied in detail to compare with those from lower luminosity systems. In this paper, we focus our attention on a particularly young outflow from an early B protostar, IRAS 20126+4104.

IRAS 20126+4104 (hereafter I20126), at $\alpha$(B1950) 20$^h$12$^m$41.0$^s$ and $\delta$(B1950) 41°04′21.0″, is located in a dark cloud in the Cygnus-X region at a kinematic distance of 1.7 pc. The far-infrared luminosity is about $10^4$ $L_\odot$, and the IRAS colors match the selection criteria for ultracompact H II regions (Wood & Churchwell 1989). The IRAS source is embedded in a 230 $M_\odot$ NH$_3$ core of roughly 0.4 pc diameter (Estalella et al. 1993) and lies close to the origin of a north-south molecular outflow (Wilking, Blackwell, & Mundy 1990). Near the center of the outflow is a bright, bipolar infrared reflection nebula with a NW-SE orientation (Hodapp 1994; Cesaroni et al. 1997, 1999, hereafter C97 and C99). In addition, a well-collimated jet from the protostar is visible in shock-enhanced SiO emission (C97, C99) and H$_2$ emission (C97, Ayala et al. 1998), while H$_2$O masers within 1″ of the source are aligned along the jet axis (Tofani et al. 1995). Observations by Kawamura et al. (1999) in the CO($J$ = 7–6) and NH$_3$(3,3) transitions imply an underlying jet density of at least $10^5$ cm$^{-3}$. A rotating 10,000 AU NH$_3$(1,1) torus with a mass of approximately 20 $M_\odot$ (Zhang, Hunter, & Sridharan 1998) surrounds a more compact disk detected in CH$_3$CN and thermal dust emission (C99; Hofner et al. 1999). The roughly 1700 AU diameter inner disk appears to lie along an axis that is nearly perpendicular to the jet axis. Near the peak of the 3 mm continuum emission, Hofner et al. (1999) have detected two elongated structures in 3.6 cm continuum emission that are within 1″ of each other. The emission is consistent with the presence of two parallel jets of ionized gas. The northern jet is elongated in the direction of the H$_2$O maser emission and is coincident with the disk inferred from CH$_3$CN emission. A disk counterpart is not detected toward the southern jet nor is there H$_2$O maser emission associated with it.

If the same young stellar object (YSO) is producing one of the inner jets with a NW-SE orientation and the north-south molecular flow, the change in position angle implies that the jet may be precessing or wandering over an angle of $\sim$40°. Jet flows from low-mass YSOs have been observed to have an S-shaped symmetry with typical opening angles $\lesssim$10°, but a jet precession angle of 40° is unusually large. It is also possible that there are multiple outflows emerging with different orientations. Clearly, high-resolution observations are needed to determine the detailed properties of I20126 and identify which scenario is correct.

We have therefore made high-resolution aperture synthesis maps of the I20126 region in CO($J$ = 1–0), $^{13}$CO(1–0), C$^{18}$O(1–0), and C$^{17}$O(1–0) to trace the dynamics of the

[1] National Radio Astronomy Observatory, 1003 Lopezville Road, Socorro, NM 87801.
[2] Division of Physics, Mathematics and Astronomy, California Institute of Technology, MS 105-24, Pasadena, CA 91125.
[3] Center for Astrophysics and Space Astronomy, CB 389, University of Colorado, Boulder, CO 80309.
[4] Osservatorio Astrofisco di Arcetri, Largo Enrico Fermi 5, I-50125 Firenze, Italy.

outflow from the large scale (1′–2′) to the small scale (inner 20″). We have also obtained images at visible, near-infrared, and mid-infrared wavelengths to provide an understanding of the shocks within the flow and the relationship between the outflow and the larger scale molecular cloud. In § 2 we describe the observations. In § 3 we present the results and point out key features of the outflow and YSO. In § 4 we discuss the flow components. We present a summary of our findings in § 5.

## 2. OBSERVATIONS

### 2.1. *OVRO Observations*

Observations in the 1.3 mm and 2.7 mm continuum, CO(1–0), $^{13}$CO(1–0), C$^{18}$O(1–0), and C$^{17}$O(1–0) lines were made with the Owens Valley Radio Observatory (OVRO) millimeter wave array of six 10.4 m telescopes between 1998 February 2 and 1999 February 3. Projected baselines ranging from 15 to 484 meters provided sensitivity to structures up to about 16″. The final $\sim 3' \times 3'$ mosaic images of both line and continuum emission consist of 13 fields with primary beam ~65″ (FWHM), spaced 30″ apart. The total integration time on source was approximately 5.3 and 2.7 hr per pointing center for the CO and $^{13}$CO/C$^{18}$O mosaics, respectively. The integration time on source at the central position was 10.5 hr for the C$^{17}$O and 3 mm continuum observations, and 2.8 hr for the 1 mm continuum observations. Cryogenically cooled SIS receivers operating at 4 K produced typical single sideband system temperatures of 200 to 600 K. Gain calibration used the quasar BL Lac and the passband calibrators were 3C 84 and 3C 273. Observations of Uranus, Neptune, and 3C 273 provided the flux-density calibration scale with an estimated uncertainty of ~20%. Calibration was carried out using the Caltech MMA data reduction package (Scoville et al. 1993). Images were produced using the MIRIAD software package (Sault, Teuben, & Wright 1995) and deconvolved with a maximum-entropy–based algorithm designed for mosaic images (Cornwell & Braun 1988). The overlap region of the mosaic is corrected for primary beam attenuation.

The spectral band pass for all lines was centered on the systemic local standard of rest velocity ($v_{\rm LSR}$) $-3.5$ km s$^{-1}$. CO emission was detected across the entire 77 km s$^{-1}$ band pass. To optimize sensitivity to extended structure, the CO *uv* data were convolved with a 6″ taper resulting in a synthesized beam of 7″.53 × 7″.09 (FWHM) at P.A. $-80$°.6. At the spectral resolution of 1.3 km s$^{-1}$, the RMS noise is 0.12 Jy beam$^{-1}$. The $^{13}$CO and C$^{18}$O *uv* data were similarly convolved, resulting in synthesized beams of 7″.46 × 6″.03 (FWHM) at P.A. $-9$°.8 and 7″.42 × 5″.85 (FWHM) at P.A. $-10$°.6, respectively. The RMS noise of the $^{13}$CO map is 65 mJy beam$^{-1}$ at spectral resolution 2.72 km s$^{-1}$, and the RMS noise in the C$^{18}$O map is 0.14 Jy beam$^{-1}$ at spectral resolution 0.68 km s$^{-1}$. The C$^{17}$O maps were convolved with a 2″ taper, which produced a synthesized beam of 3″.43 × 3″.09 (FWHM) at P.A. $-87$°.8. The RMS noise of the C$^{17}$O maps is 80 mJy beam$^{-1}$ with spectral resolution 0.67 km s$^{-1}$.

Simultaneous 3 mm continuum observations were made in a 1 GHz bandwidth channel, which for CO observations had a central frequency of 112.8 GHz and for $^{13}$CO observations had a central frequency of 113.5 GHz. The central frequency of the combined bands is 113.15 GHz. Continuum observations at 1 mm wavelength were made in two 1 GHz bands with an average frequency of 228.1 GHz. The images had a synthesized beam 2″.93 × 2″.53 (FWHM) at P.A. 78°.4 and RMS noise 1.7 mJy beam$^{-1}$ at 113 GHz and a beam of 1″.18 × 0″.81 (FWHM) at P.A. $-51$°.2 and RMS noise 19 mJy beam$^{-1}$ at 228 GHz.

### 2.2. *Mid-Infrared Observations*

Infrared images of I20126 at 12.5 and 17.9 $\mu$m were obtained on UT 1998 October 7 at the W. M. Keck Observatory[5] using the Jet Propulsion Laboratory mid-infrared camera MIRLIN mounted at the Keck II 10 m telescope. The MIRLIN focal plane array is a 128 × 128 Si:As Boeing BIB detector, with a plate scale of ~0″.14 pixel$^{-1}$, when mounted at the f/40 bent-Cassegrain focus of the Keck II telescope. The source was observed with the N5 ($\lambda_{\rm eff} \sim 12.5$ $\mu$m, $\Delta\lambda \sim 1.2$ $\mu$m) and $Q_s$ ($\lambda_{\rm eff} \sim 17.9$ $\mu$m, $\Delta\lambda \sim 2.0$ $\mu$m) filters. Data acquisition employed a chop-nod cycle with a chop frequency of ~4 Hz, and a few hundred chops per nod. Chop and nod throws of ~10″ were oriented in orthogonal directions on the sky. Background emission was subtracted by computing the double-difference of each chop-nod cycle. Final images were obtained by shifting and adding the background subtracted frames. Poor weather conditions during the observations precluded photometric calibration. The 12.5 $\mu$m image has a total exposure time of 195 s and the 17.9 $\mu$m image has a total exposure time of 12 s. The point-spread function FWHM was ~0″.4 and ~0″.5 at 12.5 and 17.9 $\mu$m, respectively. No astrometric calibration could be derived since there were no other sources within the field. To obtain an approximate position, the peak of the mid-infrared emission was assumed to be coincident with the 3 mm continuum peak. This assumption is probably accurate to within about an arcsecond.

### 2.3. *Near-Infrared Observations*

Observations in $K_s$ band and $H_2$ narrow band were taken with at the Palomar 1.5 m telescope with the Cassegrain IR Camera (IRCAM) on 1997 October 14 and 16. The Rockwell 256 × 256 HgCdTe (NICMOS-3) array has a read noise of $\sim 50\,e^-$, a pixel scale at the f/8.75 focal ratio of 0″.624 pixel$^{-1}$, and a field-of-view of 160″ (Murphy et al. 1995).[6] Images were obtained through a narrowband filter centered at 2.12 $\mu$m that includes the $H_2$ $v = 1$–0 S(1) line and a broadband $K_s$ filter [7] centered at 2.17 $\mu$m with a bandwidth of 0.33 $\mu$m (Persson et al. 1998). Ten dithered exposures were taken in each of the filters, with exposure times of 120 and 10 s in the $H_2$ and $K_s$ filters, respectively. On-source exposures were immediately followed by offsetting the telescope to a sky position. The seeing was about 1″.4 FWHM. Multiple sky frames were median combined and then subtracted from the on-source frames. After dividing by a flat field, the dithered exposures were median com-

[5] The W. M. Keck Observatory is operated as a scientific partnership among the California Institute of Technology, the University of California, and the National Aeronautics and Space Administration. The Observatory was made possible by the generous financial support of the W.M. Keck Foundation.

[6] See also E. Persson and M. Pahre 1995, Palomar 60-Inch Telescope Infrared Camera Manual, available at http://astro.caltech.edu/~eeb/p60ircam/.

[7] The $K_s$ filter has half-power transmission at ~2.0 and 2.3 $\mu$m rather than ~2.0 and 2.4 $\mu$m for the K filter. The cutoff toward the long wavelength end of the $K_s$ filter results in roughly a factor of 2 reduction in the thermal background when compared to the K filter.

bined to remove detector defects. The continuum emission in the final $H_2$ mosaic of dithered images was estimated by comparing the total flux from 15 stars in the $K_s$ and $H_2$ images, and calculating an averaged flux ratio between the two filters. The standard deviation of the measured flux ratios was $\lesssim 3\%$. The $K_s$ image was renormalized by the flux ratio and subtracted from the $H_2$ image to obtain an $H_2$ line-only image. Astrometric calibration was done by comparing common stars found in our field and the STScI Digital Sky Survey plates.

### 2.4. *Visible* Hα *and* [S II] *Observations*

We obtained images of the I20126 region on the nights of 1997 October 29–31 at the prime focus of the Mayall 4 m telescope using the engineering grade MOSAIC 8192 × 8192 CCD camera. The field of view with the imaging correctors is approximately 36′ × 36′ with a scale of 0″.26 per pixel. We obtained 600 s exposures through narrow band filters transmitting Hα and [S II]. The Hα filter is centered on 6563 Å with a band pass of 75 Å, while the [S II] filter is centered on 6723 Å with a bandpass of 80 Å. To minimize the effect of cosmetic blemishes and gaps between the individual CCDs, we centered I20126 in the middle of the best 2048 × 4096 CCD. The data was over-scanned, trimmed, dark subtracted and then flat fielded with sky flats in the standard manner using IRAF packages. The resulting full MOSAIC image still showed gaps between CCDs, and the outer areas of the image suffered from cosmetic problems that could not be calibrated out. Thus, the images presented in this paper present only the inner 6′ × 6′ field centered on the I20126 outflow.

## 3. RESULTS

### 3.1. *The I20126 Molecular Outflow*

Figures 1–5 present the large-scale morphology and kinematics of the CO outflow and the infrared and visible emission in the region. The outflow axis is predominantly north-south (position angle 171°), with redshifted gas in the south and blueshifted gas in the north. The outflow is centered near the 3 mm millimeter continuum peak (C97). From end-to-end, the flow measures 2′, which corresponds to nearly 1 pc at the distance of 1.7 kpc. The redshifted lobe is roughly twice as long as the blueshifted lobe. Velocity structure in both lobes is somewhat chaotic with a shell of low-velocity gas ($v \lesssim 10$ km s$^{-1}$) surrounding clumps of higher velocity gas ($v > 10$ km s$^{-1}$). The highest velocity redshifted gas is on the east side of the red lobe while the highest velocity blueshifted gas is located less than 10″ NW of the continuum peak.

Assuming that the flow is roughly conical in shape, the measured semiopening angle is between about 30° and 40° and there is very little overlap between the red and blue-shifted lobes. Therefore, the flow does not intersect the plane of the sky and the geometry most closely corresponds to case 2 in Cabrit & Bertout (1986) (see also Chandler et al. 1996). This indicates that a reasonable range for the inclination angle of the outflow $i$ is between 40° and 50° (measured with respect to the line of sight). Thus, we adopt the value $i = 45°$.

Near-infrared reflection nebulae are centered near the continuum source, and $H_2$ emission is within the reflection nebulae and to the NW and SE of the flow (Fig. 4, see also C97). The positions of the $H_2$ knots are listed in Table 1 and

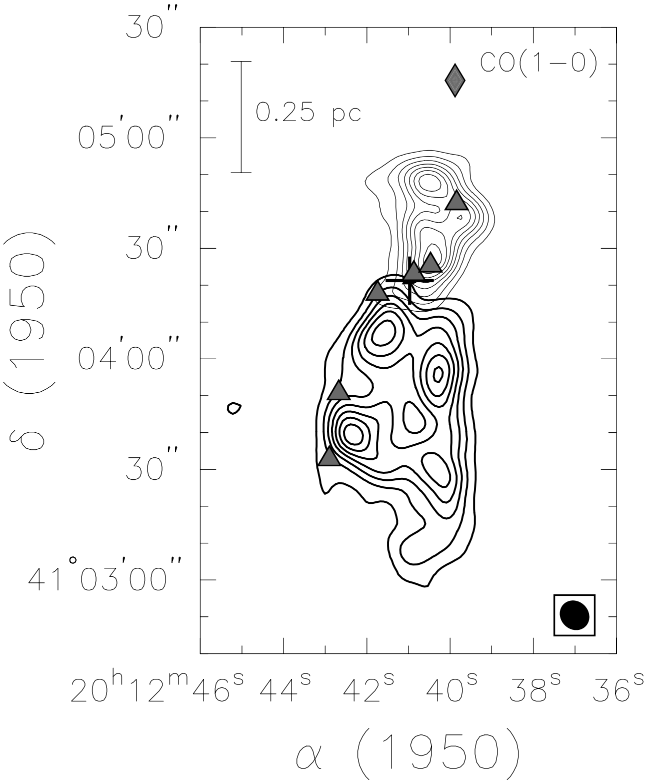


FIG. 1.—CO redshifted (*thick lines*) and blueshifted (*thin lines*) emission contours from 34.9 km s$^{-1}$ to 4.9 km s$^{-1}$ and −10.9 km s$^{-1}$ to −41.9 km s$^{-1}$, respectively. The maps have an RMS of 1.23 Jy beam$^{-1}$ km s$^{-1}$. Contours begin at 6.2 Jy beam$^{-1}$ km s$^{-1}$ (5 σ). Blueshifted contours continue with spacings of 5 σ, while redshifted contours have spacings of 10 σ. The synthesized beam, shown in the bottom right corner, is 7″.53 × 7″.09 at P.A. −80°.6. The position of the 3 mm continuum peak is indicated by a black cross. Triangles represent the locations of H2 emission knots (listed in Table 1). The diamond symbol above the blueshifted outflow lobe represents the location of the bright emission knot seen in Hα and [S II] emission. $H_2O$ maser positions identified by Tofani et al. (1995) are within 2″ of the continuum peak position and are not distinguishable on this larger scale map. A scale size of 0.25 pc is represented by the bar in the upper right.

are indicated by triangles in Figures 1 and 2. Within 10″ of the central source, the position angle of the outflow defined by the infrared emission is approximately 120°. This is consistent with position angles seen in $HCO^+$, SiO (C97, C99), $NH_3$(3,3) (Kawamura et al. 1999; Zhang et al. 1999), and ionized gas (Hofner et al. 1999). The outer $H_2$ emission knots have a more north-south orientation and appear to

TABLE 1

MEASURED POSITIONS OF $H_2$ AND [S II] EMISSION KNOTS

| Emission Knot | α(B1950) | δ(B1950) |
|---|---|---|
| $H_2$–1 .................... | 20 12 39.83 | 41 04 42.83 |
| $H_2$–2 .................... | 20 12 40.38 | 41 04 25.00 |
| $H_2$–3 .................... | 20 12 40.87 | 41 04 22.45 |
| $H_2$–4 .................... | 20 12 41.67 | 41 04 17.40 |
| $H_2$–5 .................... | 20 12 42.69 | 41 03 50.92 |
| $H_2$–6 .................... | 20 12 42.91 | 41 03 33.56 |
| Hα/[S II] ................ | 20 12 39.88 | 41 05 15.60 |

NOTE.—Units of right ascension are hours, minutes, and seconds, and units of declination are degrees, arcminutes, and arcseconds.

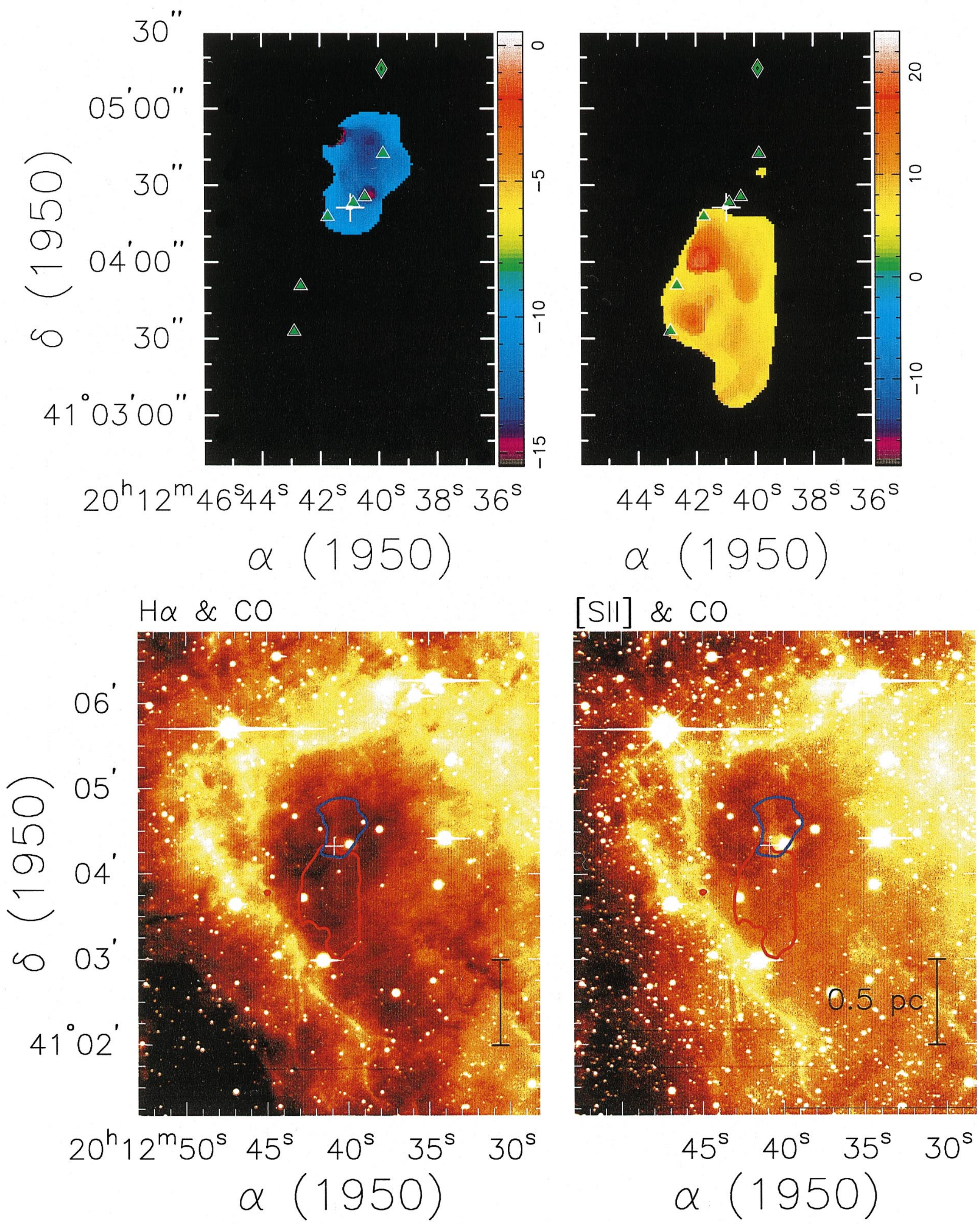


FIG. 2.—*Top:* First moment maps of the CO emission in the red and blueshifted outflow lobes. The color wedge on the right shows the velocity range. Symbols are the same as in Fig. 1. *Bottom:* Hα and [S II] emission in color scale with the lowest CO red and blueshifted emission contour from Fig. 1. The boundary of the cloud is seen as a bright rim around the cloud core. The CO outflow is seen in projection against the cloud core. The position of the 3 mm continuum peak is indicated by a cross. A scale size of 0.5 pc is represented by the bar in the lower right.

follow the boundaries of the CO outflow lobes. The two southernmost $H_2$ knots have a bright star between them suggesting that they may be associated with a different flow. However, this star has the colors of a foreground object with no significant infrared excess (C97), and no millimeter continuum emission is detected at this position (discussed in § 3.2). Thus, the southern $H_2$ knots are most likely associated with the outflow powered by I20126.

Mid-infrared emission at 12.5 and 17.9 $\mu$m is shown in Figure 5. The 17.9 $\mu$m image is also compared to the structure of $H_2$ emission near the central star. To estimate the approximate positions in the mid-IR maps, we assume the brightest peak of the mid-IR emission is coincident with the location of the millimeter continuum source (see also C99). The NW emission peak is more extended than the SE peak and the relative brightness of the NW peak increases at the longer wavelength, which may indicate a cooler temperature. The morphology and relative intensities are consistent with warm emission near the central star and either cooler dust emission or a reflection nebula stretching

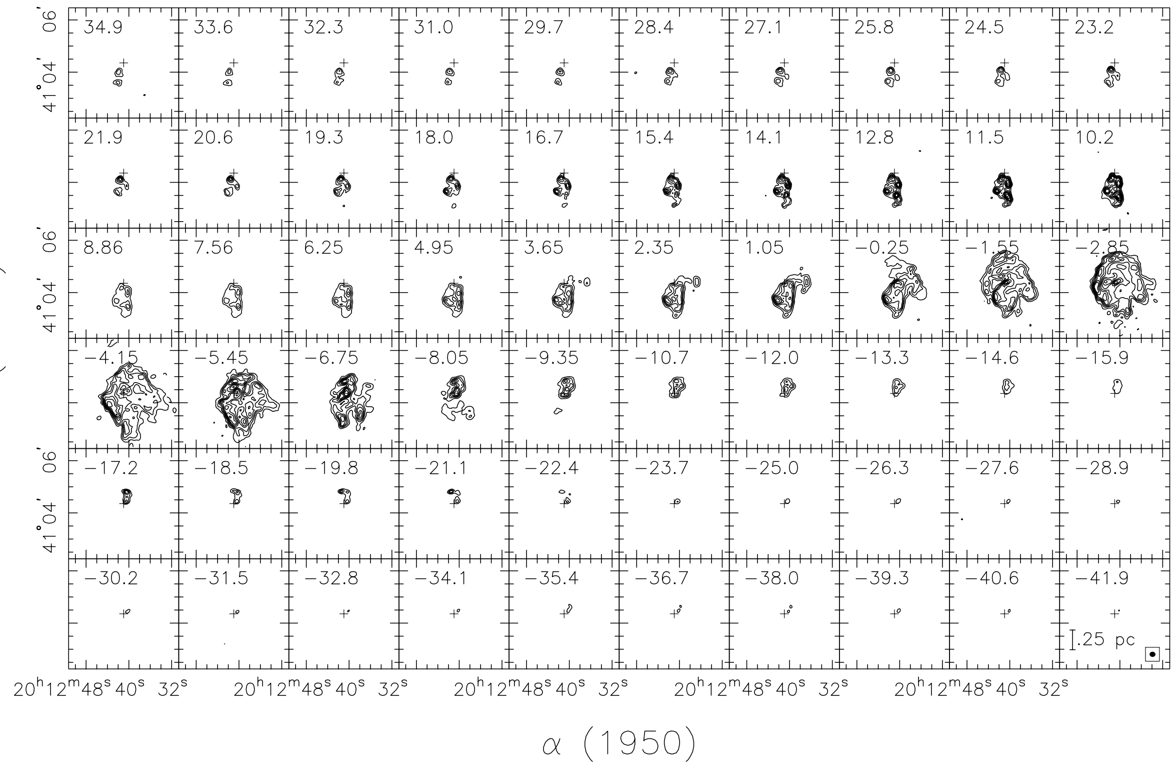


FIG. 3.—CO channel maps at 1.3 km s$^{-1}$ spectral resolution between $-41.9$ and 34.9 km s$^{-1}$. The velocity is indicated in the upper left of each panel. The RMS is 0.12 Jy beam$^{-1}$ and the peak emission is 18.5 Jy beam$^{-1}$. In the top 20 and bottom 20 panels, contours are plotted from $-5$, 5, 10, 15, 20, 25, 30, 40 $\sigma$ and continue with a spacing of 10 $\sigma$. In the central 20 panels, contours begin at $-10$, 10 $\sigma$ and continue with a spacing of 20 $\sigma$. The last panel (velocity $-41.9$ km s$^{-1}$) shows the synthesized beam in the bottom right corner (7″.53 × 7″.09 at P.A. $-80°.6$). A scale size of 0.25 pc is represented by a bar in the lower left corner. In all maps, the cross shows the position of the 3 mm continuum peak.

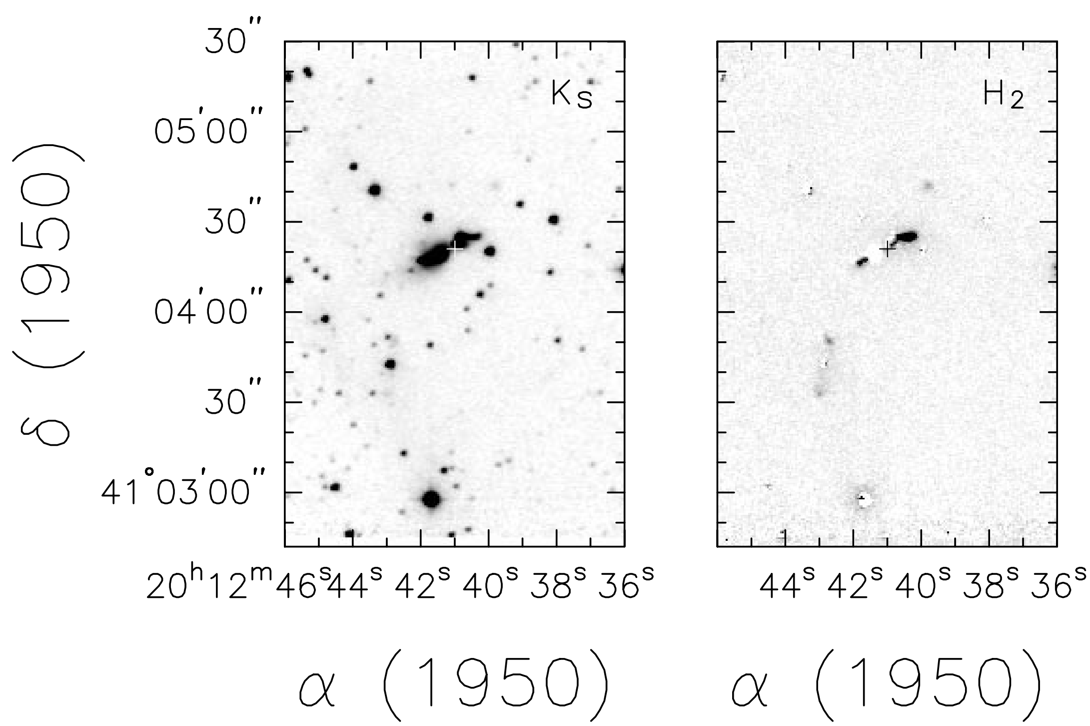


FIG. 4.—*Left:* $K_s$-band image of the bright bipolar reflection nebula centered on the millimeter continuum source. *Right:* $H_2$ line image (with continuum subtracted) showing bright $H_2$ knots within the bipolar nebula. An isolated knot is also present in the northwest, and two knots are located in the southeast. The position of the 3 mm continuum source is marked with a cross in each image.

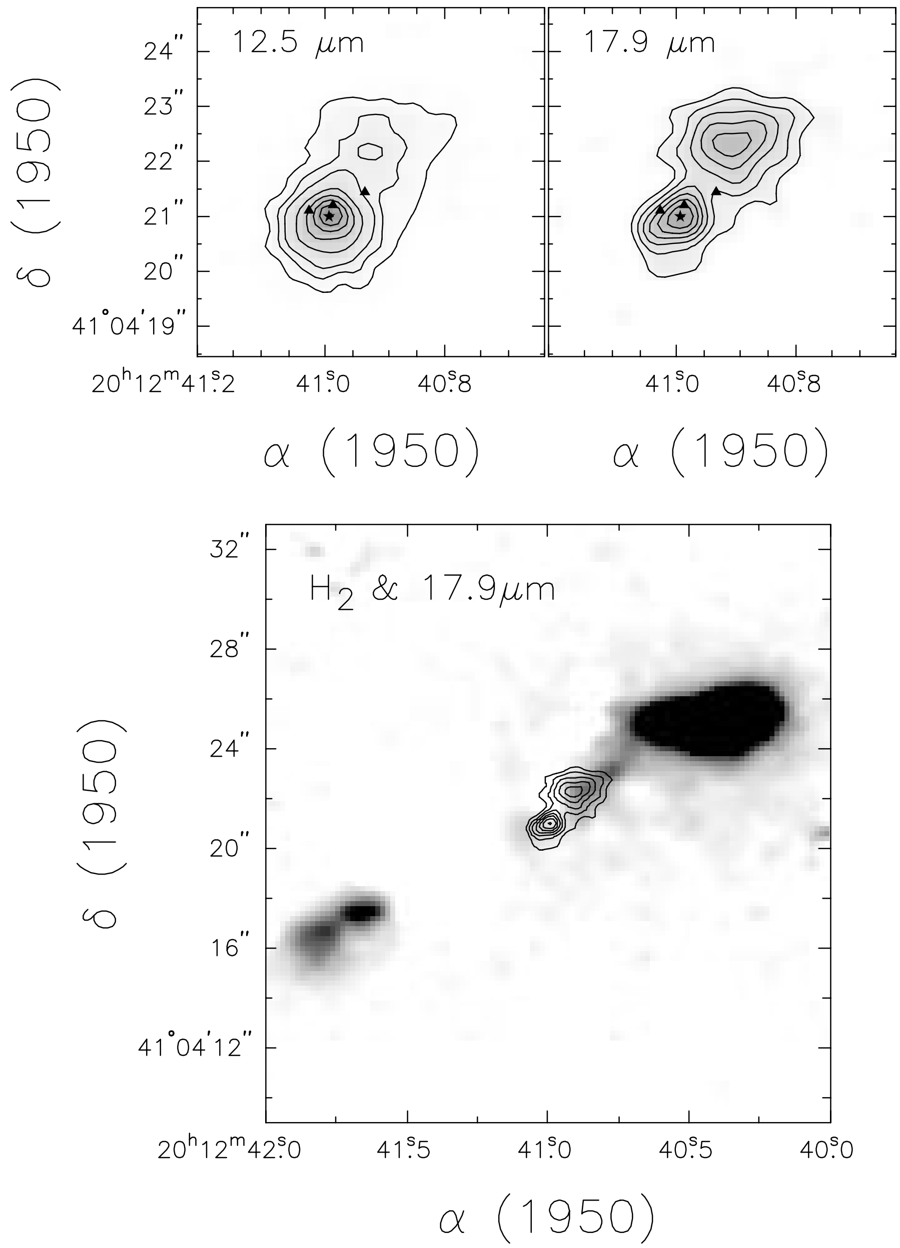


FIG. 5.—Mid-infrared images at 12.5 and 17.9 $\mu$m displayed with a gray-scale square root stretch (*top*). The 12.5 $\mu$m map RMS is 2.1 counts pixel$^{-1}$ with contours of 5, 10, 15, 20, 30, 40, 50, and 60 × RMS and the 17.9 $\mu$m map RMS is 20 counts pixel$^{-1}$ with contours of 4, 6, 8, 10, 12, 14, 16, and 18 × RMS. The three filled triangles represent $H_2O$ maser positions from Tofani et al. (1995). The filled star shows the assumed position of the millimeter continuum peak. In the bottom panel, 17.9 $\mu$m image contours are compared with the $H_2$ emission gray scale from Fig 3.

toward the blueshifted outflow lobe in the NW. Shocked $H_2$ is present within and just beyond the NW emission region.

The CO outflow is seen in projection against the larger scale molecular cloud (Fig. 2). Filamentary ridges of H$\alpha$ and [S II] emission trace the cloud boundary on three sides, and the higher extinction within the cloud is evident by the lack of background stars. The entire 36′ × 36′ MOSAIC field (not shown) is filled with a combination of diffuse and filamentary H$\alpha$ and [S II] nebulosity. The I20126 cloud is embedded in a large-scale network of [S II] bright filaments extending from northeast to the southwest across the field of view. The morphology and relatively large [S II]/H$\alpha$ ratio indicates that the filaments may trace shock fronts produced by either an old supernova remnant or possibly a very large scale superbubble. Many dark clouds are visible in silhouette against the background star field and nebulosity. Some of these clouds, including the one containing I20126 shown in Figure 2, are rimmed by ionization fronts facing toward the east indicating that hot stars illuminate the eastern rim of the I20126 cloud. Thus, it is possible that star formation in this cloud was triggered by the energy release from massive stars associated with the extended nebulosity in this portion of Cygnus.

As expected, there is little nebulosity associated with the outflow within the confines of the CO lobes owing to the high optical extinction. However, just north of the blueshifted outflow lobe is a faint, semicircular arc of H$\alpha$ and [S II] emission that resembles a bow shock and extends to the northern rim of the cloud. In the center of this "arc" of emission, an amorphous, [S II]-bright knot is visible at

$\alpha$(B1950) 20$^h$12$^m$39.88$^s$ $\delta$(B1950) 41°05′15″.6 . The position of this knot relative to the CO flow and $H_2$ emission knots is indicated by a filled diamond in Figures 1 and 2 and lies within 2° of the outflow axis determined from the CO geometry. There is also a pair of H$\alpha$ and [S II] filaments projecting beyond the southeastern rim of the cloud, below the redshifted CO lobe. We speculate that these features may correspond to portions of the CO flow that have broken free of the molecular cloud and have been dissociated or, perhaps, ionized. Our data cannot confirm this interpretation; however, H$\alpha$ spectroscopy would resolve this uncertainty.

The combined $H_2$ and [S II]-bright knots display a remarkable S-shaped symmetry about the central star. The three innermost $H_2$ knots lie along the SiO jet axis identified by C97, while the outer $H_2$ and [S II] knots show a rotation of approximately 45° relative to the jet axis.

### 3.2. *Circumstellar Material Surrounding the Central B Star*

Figure 6 presents 1 mm and 3 mm continuum images of thermal dust emission near the central star. No other continuum sources were detected in the mosaic image above a level of 3 $\sigma$ (5.1 mJy). A significant fraction of the 3 mm continuum emission is extended over a 10,000 AU diameter region as shown in the top panel of Figure 6 where all baselines were used to recover extended emission. An integrated flux density of 81.14 mJy and peak flux density of 34.7 mJy beam$^{-1}$ is found at position $\alpha$(B1950) 20$^h$12$^m$40.99 $\delta$(B1950)+41°04′21″.0. The location of the 3 mm emission peak is within 0″.4 of the position reported by C99. The integrated flux density is approximately three times larger than that found by C99 and is probably due to the larger inner hole in the Plateau de Bure (PdB) *uv* coverage, which resolves out more extended emission. The center panel of Figure 6 shows the compact 3 mm emission where much of the extended structure has been resolved out by using only longer baselines. The total flux density recovered in this map is 62.2 mJy, and the peak flux density is 20.6 mJy beam$^{-1}$. The location of the 3 mm emission peak remains the same. The central peak of the compact emission is nearly coincident with the $H_2O$ masers tracing the northern ionized jet, while the extension to the south is coincident with the southern ionized jet (Tofani et al. 1995; Hofner et al. 1999).

Figure 7 presents the spectral energy distribution (SED) of I20126 from 3.6 cm to 2.2 $\mu$m, including fluxes from the literature. The dashed line is our best-fit SED using a constant dust temperature of 44 K and a dust emissivity index, $\beta = 1.5$. The integrated bolometric luminosity $L_{\rm bol}$ is $\sim 10^4$ $L_\odot$. The estimated flux at 1 and 3 mm from free-free emission is $\sim$0.2 mJy, assuming a spectral index of $-0.1$ between 3.6 cm (Hofner et al. 1999) and millimeter wavelengths. This is well below the 1 $\sigma$ RMS of 19 and 1.7 mJy beam$^{-1}$ in the 1 and 3 mm continuum images, respectively. Thus, we assume the millimeter flux density is due to thermal dust emission. This is in good agreement with C99 and Hofner et al. (1999). Following the method of Hildebrand (1983), the mass of gas and dust is estimated from the millimeter continuum emission using $M_{\rm gas+dust} = [F_\nu D^2/B_\nu(T_d)\kappa_\nu]$ where $D$ is the distance to the source, $F_\nu$ is the continuum flux density due to thermal dust emission at frequency $\nu$, $B_\nu$ is the Planck function at temperature $T_d$. Assuming a gas-to-dust ratio of 100, the dust opacity per gram of gas is taken to be $\kappa_\nu = 0.004(\nu/245\ \mathrm{GHz})^\beta$ cm$^2$ g$^{-1}$

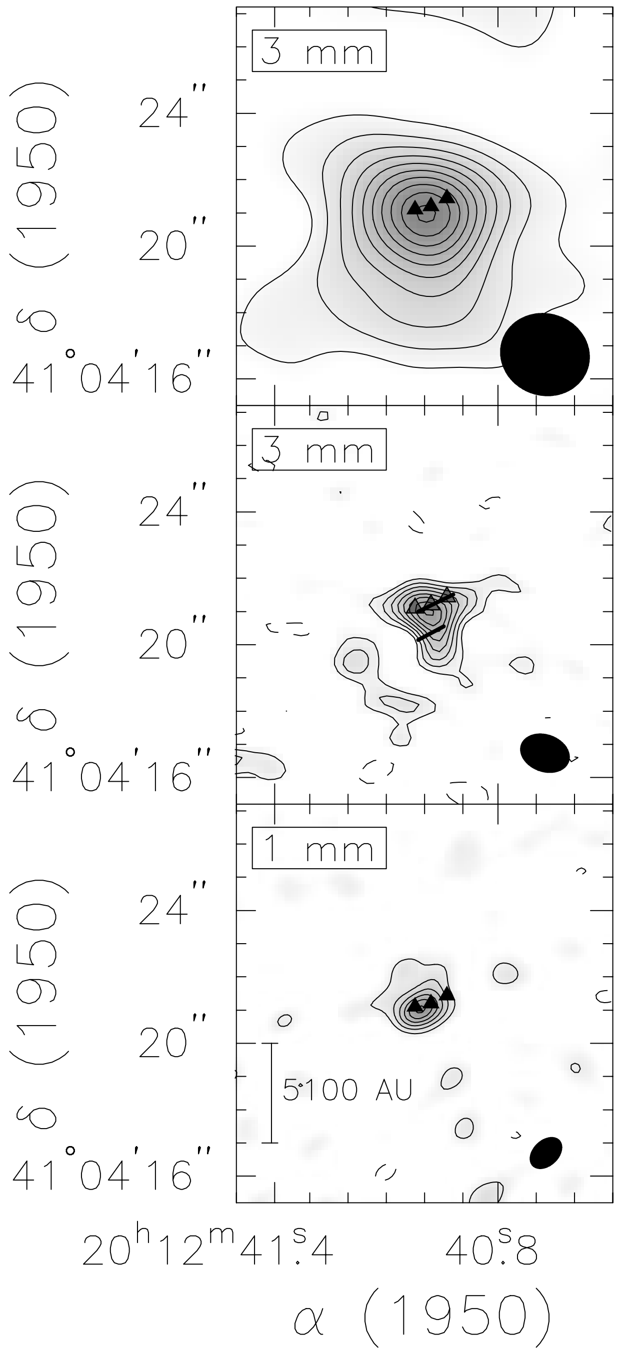


FIG. 6.—Continuum emission near the central source in I20126. The top panel shows 3 mm continuum emission using baselines ranging from 15 to 242 m. The map has an RMS of 1.7 mJy beam$^{-1}$. Contours begin at $-2$, 2, 4 $\sigma$ and continue with spacings of 2 $\sigma$. The gray scale is plotted on a linear scale from 1.7 to 3.47 mJy beam$^{-1}$. The synthesized beam is 2″.93 × 2″.53 at P.A. 78°.4. The central panel shows the 3 mm continuum emission using the longer baselines (70 to 484 m) to show the most compact emission distribution. The map has an RMS of 2.1 mJy beam$^{-1}$. Contours begin at $-2$, 2, 3 $\sigma$ and continue with spacings of 1 $\sigma$. The gray scale is plotted on a linear scale from 2.1 mJy beam$^{-1}$ to 2.06 mJy beam$^{-1}$. The synthesized beam is 1″.65 × 1″.16 at P.A. 73°.3. The bottom panel shows the 1 mm continuum emission with resolution 1″.18 × 0″.81 at P.A. $-51$°.2. The map has an RMS of 19.0 mJy beam$^{-1}$. Contours begin at $-3$, 3, 5 $\sigma$ and continue with spacings of 2 $\sigma$. The gray scale is plotted on a linear scale from 19 to 254.9 mJy beam$^{-1}$. Synthesized beams are shown in the bottom right corners of each panel. A scale size of 5100 AU is represented by the bar in the lower left. The three filled triangles near the continuum peak represent $H_2O$ maser positions from Tofani et al. (1995). In the center panel, the two thick, parallel lines represent the size and orientation of the ionized jets discovered by Hofner et al. (1999).

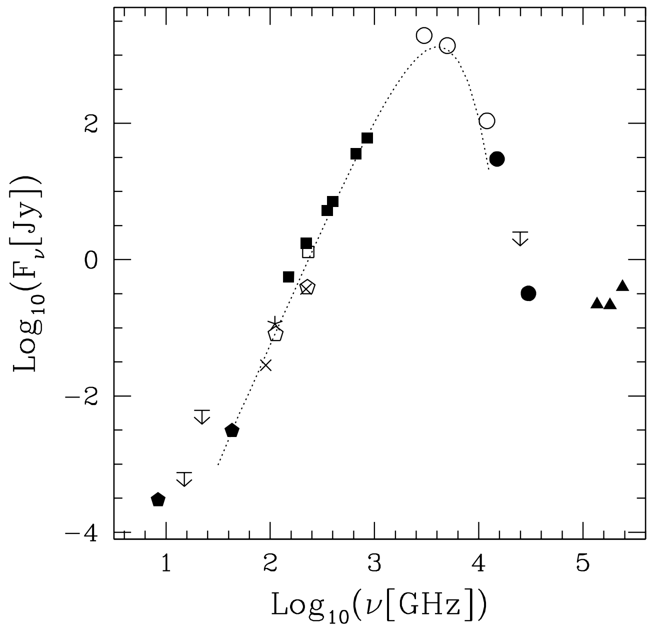


FIG. 7.—Spectral energy distribution for I20126 from 3.6 cm to 2.2 $\mu$m. The dashed line represents our best fit to the far-infrared and millimeter points with $T_d = 44$ K and $\beta = 1.5$. Symbols are (roughly from left to right): filled pentagon = VLA (Hofner et al. 1999); arrow = VLA, upper limits at 2 cm and 1.3 cm (from Wilking et al. [1989] and Tofani et al. [1995], respectively; cross = PdB (Cesaroni et al. 1999); star = OVRO (Wilking et al. 1989); open pentagon = OVRO (this work); filled square = SCUBA (Cesaroni et al. 1999); open square = NRAO-12 m (Walker, Adams, & Lada 1990); open circle = IRAS detections at 100, 60, and 25 $\mu$m; filled circle = MAX (Cesaroni et al. 1999); arrow = IRAS upper limit at 12 $\mu$m; and filled triangles = ARNICA (Cesaroni et al. 1997).

based on measurements by Kramer et al. (1998). We assume that the emission is optically thin, and the temperature of the dust can be characterized by a single value. Using values of $T_d = 44$ K and $\beta = 1.5$ determined from the SED, we find the mass of gas and dust associated with the 3 mm continuum emission is approximately 52 $M_\odot$.

The integrated flux at 1 mm is 393.9 mJy with peak flux of 254.9 mJy beam$^{-1}$ at position $\alpha$(B1950) 20$^{\rm h}$12$^{\rm m}$40$^{\rm s}$.001 $\delta$(B1950)+41°04′21″.00 (bottom panel of Fig. 6). The source is unresolved with a deconvolved size of less than 1″.06 × 0″.83 at P.A. −81°. Again, assuming $T_d = 44$ K and $\beta = 1.5$, we find that the mass of gas and dust associated with the 1 mm continuum emission is approximately 22 $M_\odot$. The size of the 1 mm emission region is significantly less than that found at 3 mm, which indicates that the more extended flux is probably resolved out. Thus, as expected, the 1 mm mass estimate is lower than that derived from the 3 mm continuum emission.

### 3.3. *Outflow Mass Estimates*

To estimate the CO optical depth in the flow and examine the dense gas morphology, mosaic images of $^{13}$CO, C$^{18}$O, and C$^{17}$O emission were also obtained along with the CO mosaic presented in § 3.1. Comparisons between the outflow morphology traced by CO and $^{13}$CO red and blueshifted gas and the C$^{18}$O integrated intensity are presented in Figure 8. Channel maps of $^{13}$CO and C$^{18}$O emission are shown in Figure 9. The remnant molecular core traced by C$^{18}$O emission is fractured and filamentary and appears to encase the outflow on most sides. In contrast, the $^{13}$CO emission near $v_{\rm LSR}$ nearly fills the mosaiced field. The morphology of the integrated C$^{17}$O emission tracing the highest density gas is shown in Figure 10. Only emission near the continuum source is detected with peak position $\alpha$(B1950) 20$^{\rm h}$12$^{\rm m}$41$^{\rm s}$.04 $\delta$(B1950)+41°04′20″.0, peak flux density 506 mJy beam$^{-1}$ km s$^{-1}$, and total flux 1.2 Jy.

The CO optical depth as a function of velocity is determined using CO and $^{13}$CO spectra that have been convolved with a 40″ beam (Fig. 11). We assume that $^{13}$CO is optically thin at all velocities, which is probably valid in the line wings; however, $^{13}$CO is likely to be optically thick in the line core. Further, C$^{18}$O cannot be used to estimate the optical depth of the $^{13}$CO emission because the two isotopes have very different morphologies over the same velocity range. Thus, mass estimates based on CO and $^{13}$CO emission within ±2.7 km s$^{-1}$ of $v_{\rm LSR}$ represent a lower limit. The optical depth at red and blueshifted velocities is estimated from the CO/$^{13}$CO ratio of the spectra centered on the red and blueshifted outflow lobes, respectively. In channels where no $^{13}$CO emission is detected, we assume that the CO is optically thin. Similarly, the spectra constructed from emission at the central position were used to estimate a lower limit to the optical depth within ±2.7 km s$^{-1}$ of $v_{\rm LSR}$. The CO line profile also shows a dip near $v_{\rm LSR}$ indicating that the line suffers from self-absorption and/or the interferometer map is missing some extended flux at lower velocities.

The mass associated with CO line emission is calculated following Scoville et al. (1986) and measuring the flux density in each velocity channel (corrected for the mosaic primary beam attenuation). We assume that the gas is in LTE, at a temperature of 44 K with [CO]/[H$_2$] = 10$^{-4}$, and [CO]/[$^{13}$CO] = 68.4, [CO]/[C$^{18}$O] = 513.4, and [CO]/[C$^{17}$O] = 2824 at the galactocentric distance of 8.1 kpc (Wilson & Rood 1994). Table 2 summarizes the physical properties of the molecular gas in the flow. The total flow mass $M_f$ is given by $\sum M_i$, momentum $P$ is $\sum M_i v_i$, and energy $E$ is $\frac{1}{2} \sum M_i v_i^2$, where $M_i$ is the flow mass in velocity channel $i$, and $v_i$ is the central velocity of the channel relative to $v_{\rm LSR}$. A characteristic flow timescale $t_d$ is $R_f/\langle V \rangle$, where $\langle V \rangle$ is $P/(\sum M_i)$ (Cabrit & Bertout 1990) and $R_f$ is the flow radius. Finally, the mass outflow rate $\dot{M}_f$ is $\sum M_i/t_d$ and force $F$ is $P/t_d$. The total molecular mass in the flow ($|v| > 2.7$ km s$^{-1}$) is approximately 53 $M_\odot$. This

TABLE 2

IRAS 20126 OUTFLOW PARAMETERS

| Parameter | Value |
|---|---|
| Distance (kpc) | 1.7 |
| CO radius of redshifted outflow (pc) | 0.64 |
| CO radius of blueshifted outflow (pc) | 0.35 |
| Inclination angle (deg) | ∼45 |
| Outflow mass (corrected for optical depth): | |
| Redshifted ($M_\odot$) | 33.2 |
| Blueshifted ($M_\odot$) | 19.8 |
| Total ($M_\odot$) | 53.0 |
| Dynamical timescale (yr) | 6.4 × 10$^4$ |
| $\dot{M}_f$ ($M_\odot$ yr$^{-1}$) | 8.1 × 10$^{-4}$ |
| Momentum ($M_\odot$ km s$^{-1}$) | 403 |
| Kinetic energy (ergs) | 5.1 × 10$^{46}$ |
| Momemtum supply rate (force) ($M_\odot$ km s$^{-1}$ yr$^{-1}$) | 6.0 × 10$^{-3}$ |
| Mechanical luminosity ($L_\odot$) | 5.9 |
| Circumstellar mass $M_{\rm (gas\ +\ dust)}$ [a] ($M_\odot$) | 52 |

[a] Based on OVRO 3 mm continuum flux.

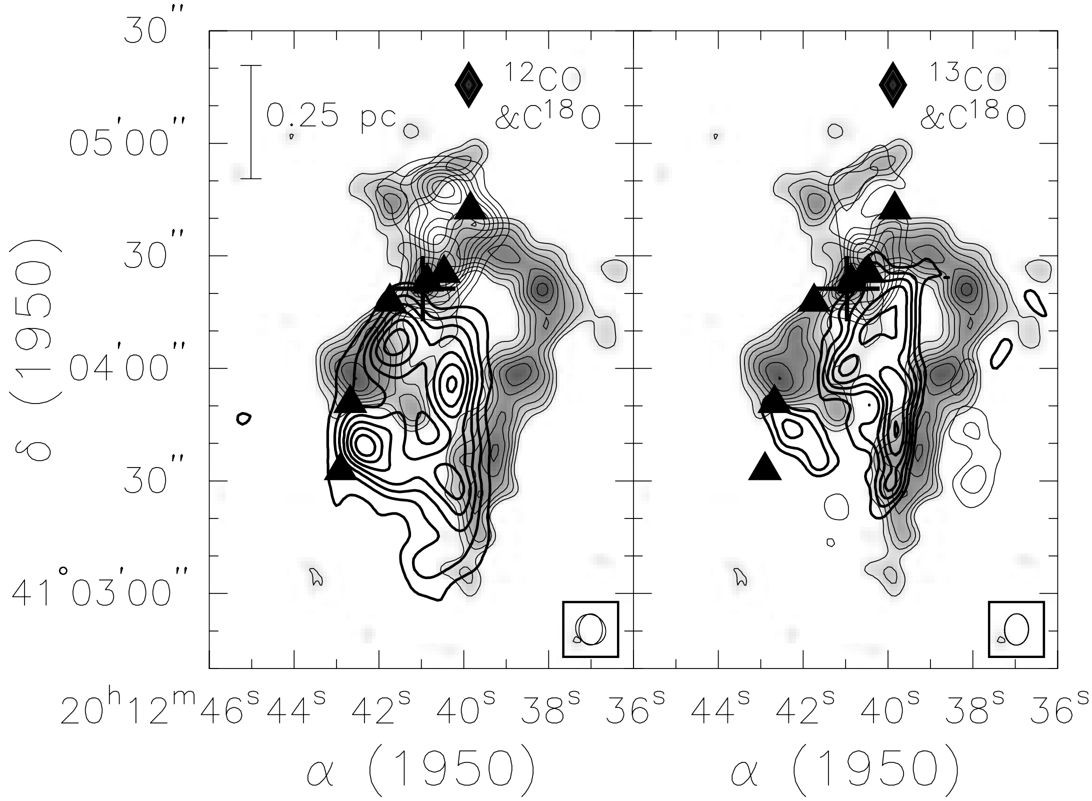


FIG. 8.—Comparison of the red and blueshifted emission in CO and $^{13}$CO with the C$^{18}$O integrated intensity. The CO contours in the left panel are from Fig. 1. $^{13}$CO redshifted (*thick lines*) and blueshifted (*thin lines*) emission contours are from 0.58 to 6.02 km s$^{-1}$ and −7.58 to −13.0 km s$^{-1}$, respectively. $^{13}$CO maps have an RMS of 0.35 Jy beam$^{-1}$ km s$^{-1}$, contours begin at 1.4 Jy beam$^{-1}$ km s$^{-1}$ (4 $\sigma$) and continue with spacings of 0.7 Jy beam$^{-1}$ km s$^{-1}$. The synthesized beam is 7″.46 × 6″.03 at P.A. −9°.8. C$^{18}$O integrated intensity map from −5.21 to −1.8 km s$^{-1}$ is shown in gray contours and gray scale. The map has an RMS of 0.27 Jy beam$^{-1}$ km s$^{-1}$, contours begin at 3 $\sigma$ and continue with spacings of 1 $\sigma$. The gray scale is plotted on a linear scale from 0.27 to 2.54 Jy beam$^{-1}$ km s$^{-1}$. The synthesized beam is 7″.42 × 5″.85 at P.A. −10°.6. Synthesized beams for each map are shown in the bottom right. Symbols are the same as in Fig. 1.

value compares reasonably well with the outflow mass estimate of 67 $M_\odot$ by Wilking et al. (1990) made with a single dish telescope. Given the differences in the assumptions above, it does not appear that the OVRO interferometer is missing a significant amount of extended emission in the outflow.

Using emission within $\pm 2.7$ km s$^{-1}$ of $v_{\rm LSR}$ within our mosaic field, we calculate a lower limit to the quiescent molecular cloud mass associated with $^{13}$CO emission to be 249 $M_\odot$. The molecular mass associated with total C$^{18}$O emission is 104.3 $M_\odot$, and the momentum and kinetic energy in the C$^{18}$O ridges is approximately 190 $M_\odot$ km s$^{-1}$ yr$^{-1}$ and $4 \times 10^{45}$ ergs, respectively. Finally, the mass associated with C$^{17}$O emission is 7.3 $M_\odot$.

The $^{13}$CO mass within $\pm 2.7$ km s$^{-1}$ of $v_{\rm LSR}$ combined with the CO outflow mass ($|v_{\rm LSR}| > 2.7$ km s$^{-1}$) represents a lower limit to the total cloud mass of $\sim 300$ $M_\odot$. Approximately 18% of the molecular cloud material is participating in the high-velocity outflow from I20126.

## 4. DISCUSSION

The I20126 CO outflow, with a mass of approximately 50 $M_\odot$, appears to be bounded on most sides by higher density gas traced by C$^{18}$O emission. The large-scale molecular flow has a north-south axis while the near-infrared reflection nebula is oriented NW-SE along the jet axis. Shocks identified by $H_2$ and [S II] emission knots trace the jet close to the source and then rotate to a more north-south orientation farther from the source following the edges of the CO flow.

### 4.1. *The Driving Source of the Molecular Outflow*

Two protostars spaced by about 1″ (1500 AU) apart lie near the center of the I20126 outflow (Hofner et al. 1999). Each source produces a separate ionized outflow with a NW-SE orientation. We detect 3 mm and 1 mm dust continuum centered on the northern source (hereafter I20126 N), and it is associated with $H_2O$ masers along the ionized jet axis (Tofani et al. 1995). I20126 N is near the center of a massive, $\sim 1700$ AU diameter disk detected in $CH_3CN$(5–4) (C99) and 7 mm continuum emission (Hofner et al. 1999). The disk has a position angle of approximately 46° that is nearly perpendicular to the ionized jet (P.A. 117°). I20126 N is also clearly the center of the outflow activity seen in $H_2$, SiO, $NH_3$, and CO($J = 7$–6) (Tofani et al. 1995; C97; Zhang et al. 1998, 1999; C99; Hofner et al. 1999; Kawamura et al. 1999). The southern ionized outflow (hereafter I20126 S) is weaker and there are no other signs of accretion disk or strong outflow activity centered on this position. Our 3 mm continuum image shows that there is warm dust emission coincident with I20126 S (center panel in Fig. 6); consistent with the presence of an embedded protostar. Saraceno et al. (1996) have shown that the millimeter flux is proportional to the bolometric luminosity of the embedded protostar. The lack of detectable 1 mm or 7 mm continuum emission and weaker 3 mm emission from I20126 S thus

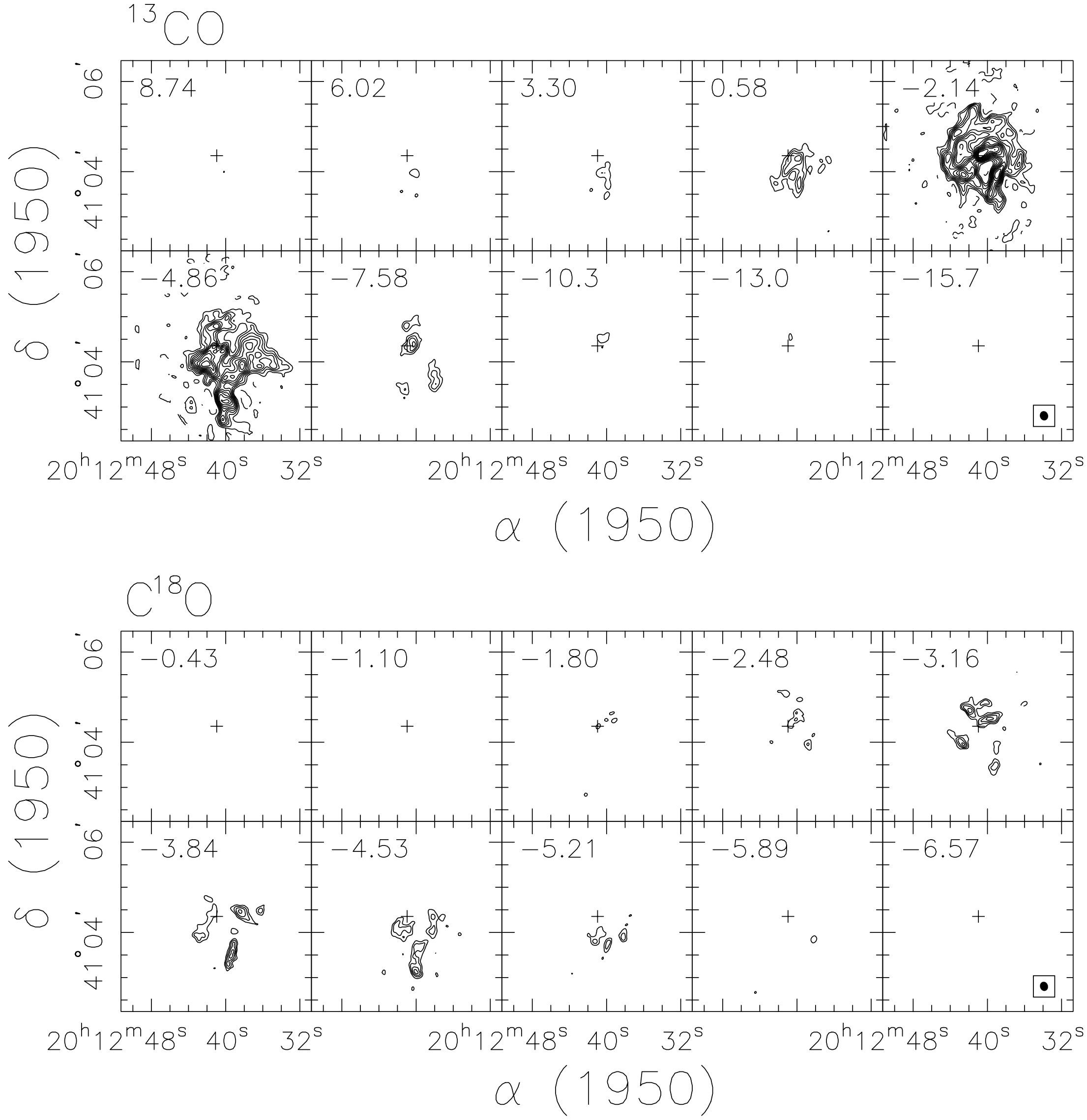


FIG. 9.—*Top:* $^{13}$CO channel maps at 2.72 km s$^{-1}$ spectral resolution between −15.7 and 8.74 km s$^{-1}$. The velocity is indicated in the upper left of each panel. The RMS is 65 mJy beam$^{-1}$ and the peak emission is 4.16 Jy beam$^{-1}$. Contours begin at −5, 5 $\sigma$ and continue with a spacing of 5 $\sigma$. The last panel (velocity = 15.7 km s$^{-1}$) shows the synthesized beam in the bottom right corner (7.″46 × 6.″03 at P.A. −9.°8). *Bottom:* C$^{18}$O channel maps at 0.68 km s$^{-1}$ spectral resolution between −6.57 and −0.43 km s$^{-1}$. The RMS is 140 mJy beam$^{-1}$ and the peak emission is 1.55 Jy beam$^{-1}$. Contours are plotted at −4, 4, 6, 8, 10, 12 $\sigma$. The synthesized beam (7.″42 × 5.″85 at P.A. −10.°6−10.6°) is shown in the last panel. The cross shows the position of the 3 mm continuum peak.

implies that the source itself is probably of lower luminosity than I20126 N. The mass outflow rate from I20126 S is also expected to be lower since outflow energetics ($\dot{M}_f$, $F$ and mechanical luminosity in the flow) scale with source luminosity (Cabrit & Bertout 1992; Shepherd & Churchwell 1996, and references therein). The scenario of a binary system with the primary having a more energetic outflow and more massive circumstellar disk with, presumably, a higher disk accretion rate is consistent with what is found for many lower mass binaries: circumprimary disks appear to have longer lifetimes and higher accretion rates than circumsecondary disks (Mathieu et al. 2000 and references therein), and this result is supported by numerical simulations of binary disk evolution (Lubow & Artymowicz 2000 and references therein). This comparison indicates that I20126 N is probably dominating the outflow energetics and luminosity.

A noteworthy property of the I20126 binary system is that both sources produce an ionized jet with approximately the same position angle of $\sim$117°. The orientation matches that of the molecular jet, however, the jet axis is rotated by approximately 54° relative to the CO outflow axis. No other continuum source that could drive the massive molecular outflow has been detected in the entire mosaiced field at 1 or 3 mm. Nor has any other potential driving source been detected in 7 mm or 3.6 cm continuum emission (Hofner et al. 1999). Thus, it appears that the 53 $M_\odot$ flow with a north-south orientation is most likely powered by one or both young stellar objects in the I20126 binary system even though the jet orientation is more NW-SE. In the remaining discussion we assume that the massive north-south outflow is dominated by the I20126 N protostar and that the contribution of the I20126 S flow to the total observed flow energetics is relatively minor. This

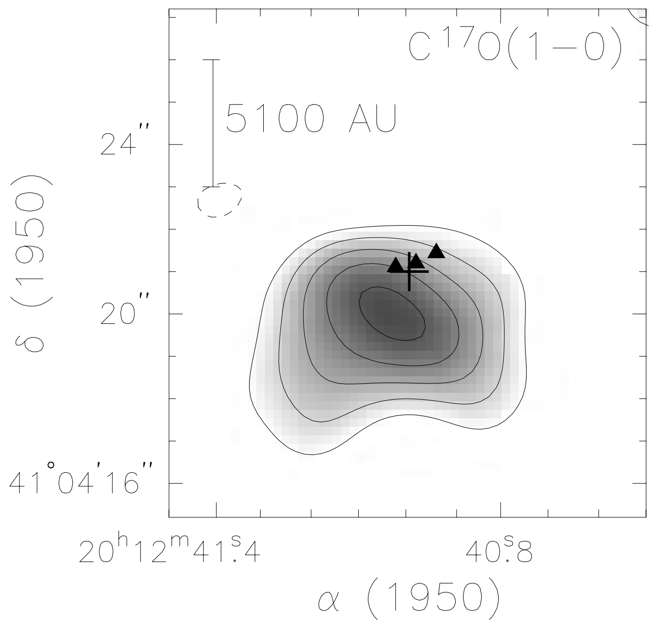


FIG. 10.—C$^{17}$O integrated intensity map from −5.5 to −3.5 km s$^{-1}$ shown in contours and gray scale. The map has an RMS of 80 mJy beam$^{-1}$ km s$^{-1}$. Contours begin at −2, 2 $\sigma$ and continue with spacings of 1 $\sigma$. The gray scale is plotted on a linear scale from 160 to 506 mJy beam$^{-1}$ km s$^{-1}$. The synthesized beam, not shown, is 3″.43 × 3″.09 at P.A. −87°.7. The position of the 3 mm continuum peak is indicated by a cross, and the $H_2O$ maser positions of C97 are denoted by solid triangles. A scale size of 5100 AU is represented by the bar in the upper left.

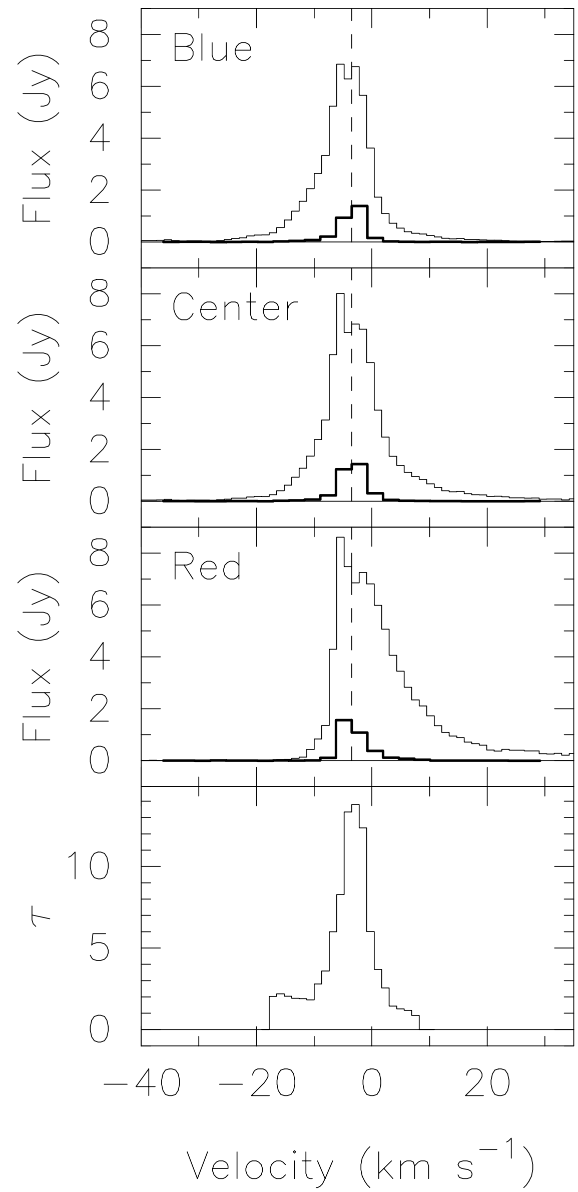


FIG. 11.—CO (*thin lines*) and $^{13}$CO (*thick lines*) spectra convolved with a 40″ beam. The top three panels show the spectra in the blueshifted lobe (20$^h$12$^m$40$^s$ 41°04′35″ B1950), on the center position (20$^h$12$^m$41$^s$ 41°04′21″) and in the redshifted lobe (20$^h$12$^m$40$^s$ 41°03′51″), respectively. The vertical dashed line shows $v_{LSR} = -3.5$ km s$^{-1}$. The bottom panel shows the optical depth derived from the spectra above.

assumption should not introduce a significant error since a low-mass star of the same kinematic age as the I20126 outflow (6.4 × 10$^4$ yr) with an average $\dot{M}_f$ of 10$^{-7}$ to 10$^{-6}$ $M_\odot$ yr$^{-1}$ would produce an outflow mass of only 0.006–0.06 $M_\odot$. This would contribute less than 0.1% to the total mass of the flow and would not likely be distinguished within the energetic lobes of a 53 $M_\odot$ outflow.

The mass outflow rate $\dot{M}_f \sim 8.1 \times 10^{-4}$ $M_\odot$ yr$^{-1}$ provides a means to obtain a rough estimate of the expected bolometric luminosity of I20126 N (Shepherd & Churchwell 1996). The measured $\dot{M}_f$ implies an $L_{bol}$ of the driving star of about 1300 $L_\odot$, which corresponds to a B3.5 spectral type (Thompson 1984). In comparison, the bolometric luminosity determined from the SED is $\sim 10^4$ $L_\odot$. The large difference between $L_{bol}$(total) and the expected $L_{bol}$ of the driving source supports the conclusion by C99 that most of the luminosity in the system may be due to accretion. Thus, the outflow parameters are consistent with a scenario in which a mid to early-B type star with $L_{bol} \sim 1300$ $L_\odot$ is driving the flow while most of the luminosity is produced by accretion.

### 4.2. *The Nature of the Jet*

We suggest that the H$\alpha$ and [S II] emission arc and central knot trace shocks associated with a high-velocity component of the blueshifted outflow that is breaking out of the near-side of the cloud. The combined $H_2$ and [S II]-bright knots display an S-shaped symmetry about the central star. The three innermost $H_2$ knots lie along the SiO jet axis while the outer $H_2$ and [S II] knots show a rotation of approximately 45° relative to the jet axis. One possible explanation for this is that the entire lobe could be filled with strong, shock-excited emission and the observed knots are simply regions in which the extinction is relatively low. However, it is not likely that such well-defined symmetry in the knot placement would exist if they were simply caused by random extinction. Further, to explain the disparate orientations of the north-south CO flow and NW-SE jet produced by a single source, one would have to invoke the special and somewhat unlikely geometry that the CO outflow must be redirected by dense cloud material in a symmetric manner for both the red and blueshifted lobes. Thus, although extinction is clearly an important factor that determines whether visible or infrared emission is present, it does not appear to be the primary cause of the S-shaped symmetry in the knots.

A more promising explanation is that the $H_2$ and [S II] knots trace the working surfaces of the I20126 N jet, as is the case for many outflows from lower mass young stellar objects (e.g., Davis, Mundt, & Eislöffel 1994; Bally et al.

1995; Zinnecker, McCaughrean, & Rayner 1997). $H_2$ is also often observed as bright bow shocks at the ends of jet flow segments and as fainter emission along the flow axis. Spectroscopic studies of the kinematics of $H_2$ and CO indicate that this happens mostly via prompt entrainment in the leading bows and to some extent via turbulent entrainment in shear layers along the flow axis (Eislöffel 1997, and references therein). Although the situation is less clear for massive outflows because the morphology is often more complex, it appears that $H_2$ may trace a steady jet in the W75 N flow (Davis et al. 1998). Assuming that the $H_2$ traces the path of the I20126 N jet, then the jet appears to be precessing through an angle of about 45°.

Independent evidence that supports a large jet precession angle in I20126 N comes from estimates of the inclination angle of the flow. A model of the SiO jet shows that the inclination angle is approximately 10° with respect to the plane of the sky (C99). The kinematic age of the jet is only about 2000 yr old; thus $i = 10°$ provides an estimate of the current inclination of the jet. In contrast, the CO outflow with $i \sim 45°$ represents the time-averaged inclination angle over the $6 \times 10^4$ yr lifetime of the molecular flow. Assuming the lobes are roughly symmetric about the flow axis, the inclination angle of the CO flow could not be significantly less than 40° without producing overlapping red and blueshifted emission in each outflow lobe. The difference of more than 30° between the inclination of the young jet and the time-averaged molecular flow is consistent with the presence of a strongly precessing jet.

### 4.3. *What Can Cause a Disk/Jet System to Precess by 45°?*

Some outflows from low-mass young stellar objects show "wiggling" knots that can be interpreted as resulting from a precessing jet. The angle of jet precession is generally less than about 10° (e.g., Bally, Devine, & Reipurth 1996; Eislöffel & Mundt 1997; Gueth & Guilloteau 1999), although a jet precession angle of ~40° is observed from the low luminosity source in L1228 (Bally et al 1995) and a jet with a 45° precession angle is observed in the from the Herbig Ae/Be star PV Ceph (Reipurth, Bally, & Devine 1997; Gomez, Kenyon, & Whitney 1997). Fendt & Zinnecker (1998) summarize proposed bending mechanisms of protostellar jets seen in low-mass flows. They conclude that two mechanisms, in particular, can create jet precession angles ~1° to 2°: precession due to a binary companion in a coplanar orbit and Lorentz forces between the electric current in the ionized jet and an interstellar magnetic field. However, precession angles greater than a few degrees cannot be generated with these mechanisms.

For more luminous systems, significantly larger precession angles (up to 90°) could be generated through radiation-induced warping of protostellar accretion disks if the disk is illuminated by a sufficiently strong central radiation source (Armitage & Pringle 1997). Dramatic changes in the jet orientation could also be caused by anisotropic accretion events, and precession could be induced by tidal interactions between the disk from which the outflow originates and a close companion star in a noncoplanar orbit (e.g., Terquem et al. 1999 and references therein). Here we consider each possibility to determine if the scaled parameters of a massive star and cloud core would create a larger jet precession angle.

*Radiative-induced warping.*—If the accretion disk is significantly warped near the star where the jet is produced, and the jet remains perpendicular to the surface of the warped disk, then the jet would precess as the system rotates. To examine whether the I20126 N disk is likely to be unstable to radiative warping, we follow the method of Armitage & Pringle (1997). We assume the disk is optically thick, geometrically thin, and in Keplerian rotation. In general, if the luminosity is mostly derived from accretion within the disk and boundary layer, then the disk is expected to be stable against warping. However, if the mass flux is a strongly decreasing function of radius, the outer parts of the disk could be warped by the stronger radiation emitted from the inner disk. In the extreme case, we assume all luminosity is generated at or near the surface of the star. The critical radius beyond which the disk is unstable to warping is given by

$$R_{\rm crit} = 3\eta^2\left(\frac{M_*}{M_\odot}\right)\left(\frac{\dot{M}_{\rm acc}}{10^{-9}\ M_\odot\ {\rm yr}^{-1}}\right)^2\left(\frac{L_*}{10\ L_\odot}\right)^{-2}\ {\rm AU}\ , \quad (1)$$

where $\eta$ is the ratio of the $(R, z)$ component of the disk viscosity to the $(R,\phi)$ component of the disk viscosity and $\dot{M}_{\rm acc}$ is the mass accretion rate. We assume $\eta = 1$ to obtain a rough estimate, although $\eta$ could be an order of magnitude different if the turbulence in the disk is anisotropic (Pringle 1992). If $\eta = 10$, then our estimate of $R_{\rm crit}$ would increase by a factor of 100. For I20126 N, $L_* \approx 10^4\ L_\odot$, $M_* \approx 10\ M_\odot$, and we take $\dot{M}_{\rm acc} \sim 10^{-3}\ M_\odot\ {\rm yr}^{-1}$ (C99). We find $R_{\rm crit} \sim 3 \times 10^7$ AU. For disk radii less than $R_{\rm crit}$, the disk is expected to be stable to warping. This is significantly larger than the expected disk radius of ~800 AU, thus, radiation does not appear to be able to warp the inner disk of I20126 N and cause the jet to precess.

*Anisotropic accretion events.*—Young, early B-type stars are usually surrounded by a dense cluster of lower mass stars (Testi, Palla, & Natta 1999). Thus, it is likely that I20126 N formed in the presence of lower mass condensations that could have evolved to be lower mass stars or they could have merged or interacted with the more massive I20126 N protostar (see, e.g., Bonnell, Bate, & Zinnecker 1998; Stahler, Palla, & Ho 2000 and references therein). If a collision between a condensation and a massive YSO disk occurs during an anisotropic accretion event, then it is possible the disk could be reoriented. To obtain a rough estimate of the angular momentum likely to reside in a disk around I20126 N, we assume the disk has a radius of 800 AU and is in Keplerian rotation about a 10 $M_\odot$ central star with a disk mass of ~4 $M_\odot$ (roughly 10% of the mass detected in thermal dust emission). The total angular momentum in the disk would be $\sim 2.3 \times 10^{55}$ g cm$^2$ s$^{-1}$. In a dramatic scenario, we consider a 1 $M_\odot$ condensation impacting the disk at a radius of 800 AU and velocity 5 km s$^{-1}$. The angular momentum of the impactor would be $L_{\rm impact} \sim 1.2 \times 10^{55} \sin\phi$ g cm$^2$ s$^{-1}$ where $\phi$ is the angle between the impactor trajectory and the disk plane. If $\phi = 90°$ and the impactor angular momentum is totally absorbed by the disk, the disk angular momentum vector would be reoriented by roughly $\theta = \tan^{-1}(L_{\rm impact}/L_{\rm disk}) \sim 30°$. Thus, an anisotropic accretion event of this magnitude could explain the large jet precession angle observed in the I20126 N outflow.

*Tidal interactions due to a companion in a noncoplanar orbit.*—The secondary star in a binary YSO system could produce tidal forces that act to truncate and distort the disk (Lubow & Artymowicz 2000), and it can cause the circumprimary disk to precess about the orbital axis (e.g., Terquem et al. 1999). The exact dynamics of the I20126 N disk/jet precession will depend upon the stellar masses, the orbital radius of the binary, the circumstellar and circumbinary disk masses and radii, as well as the period of precession. Making some very simplistic assumptions, our data allow us to estimate if this scenario can cause a disk precession of order of tens of degrees. Assuming the disk precesses as a rigid body and the disk surface density is uniform, the precession frequency of a Keplerian disk can be expressed as

$$\omega_p = -\frac{15}{32}\frac{M_s}{M_p}\left(\frac{R}{D}\right)^3 \cos\delta \sqrt{\frac{G\,M_p}{R^3}}\,(1-e^2)^{-3/2}\,, \quad (2)$$

where $M_s$ is the mass of the secondary, $M_p$ is the mass of the primary, $R$ is the disk radius, $D$ is the semimajor axis of the binary, $e$ is the orbital eccentricity, and $\delta$ is the angle between the disk plane and the orbit of the secondary (Terquem et al. 1999).

The morphology of the $H_2$ and [S II] knots suggest that less than or on the order of half a precession period has been completed over the $6 \times 10^4$ yr age of the outflow. Thus, as a rough estimate, the period of the precession is approximately $1.2 \times 10^5$ yr, which corresponds to a precession frequency of $-1.6 \times 10^{-12}$ s$^{-1}$. We take $R = 800$ AU (C97), $D = 1400$ AU (Hofner et al. 1999), and $M_p \sim 10$ $M_\odot$ (corresponding to a mid to early B star). We find that $M_s \cos\delta \approx 9(1-e^2)^{3/2}$ $M_\odot$. For the case of circular orbits ($e = 0$), the secondary must have roughly the same mass as the primary to induce the observed jet precession. If the orbit is highly eccentric with $e = 0.75$, then a significantly lower mass star $M_s \cos\delta \approx 2.6$ $M_\odot$ could produce the observed precession in the I20126 N jet. Although these values can serve only as an order of magnitude estimate, they are reasonable for what is expected in a cluster of massive stars. Thus, the jet precession could be caused by the presence of the binary companion if it is in a noncoplanar orbit.

More sensitive and higher resolution 1 mm and 7 mm continuum observations to estimate the circumstellar mass around the secondary would be useful to help constrain the system parameters and verify which interpretation, anisotropic accretion or a binary in a noncoplanar orbit, is the correct one.

## 5. SUMMARY

The massive molecular outflow from the I20126 region appears to be dominated by a single early B-type protostar (I20126 N) with $L_* \sim 10^3$ $L_\odot$, while most of the total luminosity of the system ($\sim 10^4$ $L_\odot$) is likely produced by accretion. Approximately 1500 AU from I20126 N is another source (I20126 S) with centimeter emission that is consistent with the presence of an ionized jet, yet there is little indication of additional outflow activity. Based on the absence of 1 mm and 7 mm continuum emission, weaker 3 mm emission, and no detectable molecular outflow, we conclude that I20126 S is less luminous than I20126 N. Thus, I20126 N is likely producing both the north-south molecular flow and the inner jet oriented along a NW-SE axis. Shocks identified by $H_2$ and [S II] emission knots appear to trace the jet as it precesses through a 45° angle. Although I20126 S does not appear to contribute significantly to the observed outflow kinematics, it may produce strong enough tidal forces that cause the circumprimary disk to precess about the orbital axis and, in turn, cause the observed jet to precess by an angle of 45° over the life time of flow. Alternatively, jet precession could be induced by a dramatic, anisotropic accretion event that alters the angular momentum vector of the disk. Additional observations are needed to determine which explanation is correct.

Research at the Owens Valley Radio Observatory is supported by the National Science Foundation through NSF grant number AST 96-13717. Star formation research at Owens Valley is also supported by NASA's Origins of Solar Systems program, Grant NAG W-4030, and by the Norris Planetary Origins Project. We would like to thank D. Koerner, B. Goodrich, and the Jet Propulsion Laboratory MIRLIN team for their help with the Keck mid-infrared observations, A. Sargent for critically reading an early version of the manuscript, and the referee, R. Bachiller, for useful comments that improved this paper.

## REFERENCES

Armitage, P. J., & Pringle, J. E. 1997, ApJ, 488, L47
Ayala, S., Curiel, S., Raga, A. C., Noriega-Crespo A., & Salas, L. 1998, A&A, 332, 1055
Bachiller, R., & Tafalla, M. 1999, in The Origins of Stars and Planetary Systems, ed. C. Lada & N. Kylafis (NATO ASI Ser. C, 540; Dordrecht: Kluwer), 227
Bally, J., Devine, D., Fesen, R. A., & Lane, A. P. 1995, ApJ, 454, 345
Bally, J., Devine, D., & Reipurth, B. 1996, ApJ, 473, L49
Bonnell, I. A., Bate, M. R., & Zinnecker, H. 1998, MNRAS, 298, 93
Cabrit, S., & Bertout, C. 1986, ApJ, 307, 313
———. 1990, ApJ, 348, 530
———. 1992, A&A, 261, 274
Cabrit, S., Raga, A., & Gueth, F. 1997, in IAU Symp. 182, Herbig-Haro Flows and the Birth of Stars, ed. B. Reipurth & C. Bertout (Dordrecht: Kluwer), 163
Cesaroni, R., Felli, M., Jenness, T., Neri, R., Olmi, L., Robberto, M., Testi, L., & Walmsley, C. M. 1999, A&A, 345, 949 (C99)
Cesaroni, R., Felli, M., Testi, L., Walmsley, C. M., & Olmi, L. 1997, A&A, 325, 725 (C97)
Chandler, C. J., Tereby, S., Barsony, M., Moore, T. J. T., & Gautier, T. N. 1996, ApJ, 471, 308
Cornwell, T., & Braun, R. 1988, in ASP Conf. Ser. 6, Synthesis Imaging in Radio Astronomy, ed. R. A. Perley, F. R. Schwab, & A. H. Bridle (San Francisco: ASP), 167
Davis, C. J., Mundt, R., & Eislöffel, J. 1994, ApJ, 437, L55
Davis, C. J., Smith, M. D., & Moriarty-Schieven, G. H. 1998, MNRAS, 299, 825
Eislöffel, J. 1997, in IAU Symp. 182, Herbig-Haro Outflows and the Birth of Low Mass Stars, ed. B. Reipurth & C. Bertout (Dordrecht: Kluwer), 93
Eislöffel, J., & Mundt, R. 1997, AJ, 114, 280
Eislöffel, J., Mundt, R., Ray, T. P., & Rodríguez, L. F. 2000, in Protostars and Planets IV, ed. V. Mannings, A. P. Boss, & S. S. Russell (Tucson: Univ. Arizona Press), in press
Estalella, R., Mauersberger, R., Torrelles, J. M., Anglada, G., Gómez, J. F., López, R., & Muders, D. 1993, ApJ, 419, 698
Fendt, C., & Zinnecker, H. 1998, A&A, 334, 750
Gomez, M., Kenyon, S. J., & Whitney, B. A. 1997, AJ, 114, 265
Gueth, F., & Guilloteau, S. 1999, A&A, 343, 571
Hildebrand, R. H. 1983, QJRAS, 24, 267
Hodapp, K.-W. 1994, ApJS, 94, 615
Hofner, P., Cesaroni, R., Rodríguez, L. F., & Martí, J. 1999, A&A, 345, L43
Kawamura, J. H., Hunter, T. R., Tong, C.-Y. E., Blundell, R., Zhang, Q., Katz, C. A., Papa, D. C, & Sridharan, T. K. 1999, PASP, 111, 1088
Königl, A., & Pudritz, R.E. 2000, in Protostars and Planets IV, ed. V. Mannings, A. P. Boss, & S. S. Russell (Tucson: Univ. Arizona Press), in press
Kramer, C., Alves, J., Lada, C., Lada, E., Sievers, A., Ungerechts, H., & Walmsley, M. 1998, A&A, 329, L33
Lubow, S., & Artymowicz, P. 2000, in Protostars and Planets IV, ed. V. Mannings, A. P. Boss, & S. S. Russell (Tucson: Univ. Arizona Press), in press

Mathieu, R. D., Ghez, A. M., Jensen, E. L. N., & Simon, M. 2000, in Protostars and Planets IV, ed. V. Mannings, A. P. Boss, & S. S. Russell (Tucson: Univ. Arizona Press), in press
Murphy, D. C., Persson, S. E., Pahre, M. A., Sivaramakrishnan, A., & Djorgovski, S. G. 1995, PASP, 107, 1234
Persson, S. E., Murphy, D. C., Krzeminski, W., Roth, M., & Rieke, M. J. 1998, AJ, 116, 2475
Pringle, J. E. 1992, MNRAS, 258, 811
Reipurth, B., Bally, J., & Devine, D. 1997, AJ, 114, 2708
Richer, J. S., Shepherd, D. S., Cabrit, S., Bachiller, R., & Churchwell, E. 2000, in Protostars and Planets IV, ed. V. Mannings, A. P. Boss, & S. S. Russell (Tucson: Univ. Arizona Press), in press
Rodríguez, L. F., Rev. Mex. Astron. Astrofis. Conf. Ser. 1, Circumstellar Disks, Outflows, and Star Formation, ed. S. Lizano & J. M. Torrelles, 1
Saraceno, P., André, P., Ceccarelli, C., Griffin, M., Molinari, S. 1996, A&A, 309, 827
Scoville, N. Z., Sargent, A. I., Sanders, D. B., Claussen, M. J., Masson, C. R., Lo, K. Y., & Phillips, T. G. 1986, ApJ, 303, 416
Sault, R. J., Teuben, P. J., & Wright, M. C. H. 1995, in ASP Conf. Ser. 77, Astronomical Data Analysis Software and Systems IV, ed. R. A. Shaw, H. E. Payne, & J. J. E. Hayes (San Francisco: ASP), 433
Scoville, N. Z., Carlstrom, J. E., Chandler, C. J., Phillips, J. A., Scott, S. L., Tilanus, R. P. J., & Wang, Z. 1993, PASP, 105, 1482
Shepherd, D. S., & Churchwell, E. 1996, ApJ, 472, 225
Shu, F. H., Najita, J. R., Shang, H., & Li, Z.-Y. 2000, in Protostars and Planets IV, ed. V. Mannings, A. P. Bo & S. S. Russell (Tucson: Univ. Arizona Press), in press
Stahler, S. W., Palla, F., & Ho, P. T. P., in Protostars and Planets IV, ed. V. Mannings, A. P. Boss, & S. S. Russell (Tucson: Univ. Arizona Press), in press
Terquem, C., Eislöffel, J., Papaloizou, J. C. B., & Nelson, R. P. 1999, ApJ, 512, L131
Testi, L., Palla, F., & Natta, A. 1999, A&A, 342, 515
Thompson, R. I. 1984, ApJ, 283, 165
Tofani, G., Felli, M., Taylor, G. B., & Hunter, T. R. 1995, A&AS, 112, 299
Walker, C. K., Adams, F. C., & Lada, C. J. 1990, ApJ, 349, 515
Wilking, B. A., Mundy, L. G., Blackwell, J. H., & Howe, J. E. 1989, ApJ, 345, 257
Wilking, B. A., Blackwell, J. H., & Mundy, L. G. 1990, AJ, 100, 758
Wilson, T. L., & Rood, R. T. 1994, ARA&A, 32, 191
Wood, D. O. S., & Churchwell, E. 1989, ApJ, 340, 265
Zhang, Q., Hunter, T. R., & Sridharan, T. K. 1998, ApJ, 505, L151
Zhang, Q., Hunter, T. R., Sridharan, T. K., & Cesaroni, R. 1999, ApJ, 527, 117
Zinnecker, H., McCaughrean, M., & Rayner, J. 1997, in Low-Mass Star Formation from Infall to Outflow, ed. F. Malbet & A. Castets (Grenoble: Obs. Grenoble), 198